J. Fluid Mech. (1990), *vol.* 217, *pp.* 639–660
Printed in Great Britain

Energy stability of thermocapillary convection in a model of the float-zone crystal-growth process

By Y. SHEN[1], G. P. NEITZEL[1], D. F. JANKOWSKI[1] AND H. D. MITTELMANN[2]

[1] Department of Mechanical and Aerospace Engineering, Arizona State University, Tempe, AZ 85287, USA

[2] Department of Mathematics, Arizona State University, Tempe, AZ 85287, USA

(Received 24 July 1989 and in revised form 30 January 1990)

Energy stability theory has been applied to a basic state of thermocapillary convection occurring in a cylindrical half-zone of finite length to determine conditions under which the flow will be stable. Because of the finite length of the zone, the basic state must be determined numerically. Instead of obtaining stability criteria by solving the related Euler–Lagrange equations, the variational problem is attacked directly by discretization of the integrals in the energy identity using finite differences. Results of the analysis are values of the Marangoni number, Ma_E, below which axisymmetric disturbances to the basic state will decay, for various values of the other parameters governing the problem.

1. Introduction

Thermocapillary convection is a fluid motion driven by surface-tension gradients on a liquid–gas interface, where these gradients arise from surface-temperature gradients and the temperature dependence of surface tension. This type of convection plays an important role in many technological and scientific applications; interesting examples may be found in the field of materials processing, particularly crystal-growth processes in which bulk melts are found. One such crystal-growth process is the so-called 'float-zone' technique by which high-purity electronic materials (notably silicon) can be produced. In this method a rod of polycrystalline material is moved slowly through a heating device which melts a portion of it. Ideally, as the melt resolidifies it does so as a single crystal which is then used as substrate for building microelectronic devices. Since the method is containerless, the possibility of contamination by contact with other materials is reduced. However, because surface-tension forces must support the weight of the material contained in the zone, the size of the resulting crystal is limited in Earth-based production; in fact, some materials have properties which prevent this process from being used to manufacture crystals of reasonable size. Consequently, a microgravity environment such as that provided by the Space Shuttle has been suggested as a possible site for growing bigger, and hopefully better, crystals.

In addition to allowing larger crystals to be grown, a microgravity environment would also significantly reduce the magnitude of convection induced by buoyancy forces. This convection was once thought to be at least partly responsible for the presence of undesirable non-uniformities in material properties called *striations* observed in float-zone material. Recent speculation, however, is that the onset of time-dependent thermocapillary convection (Preisser, Schwabe & Scharmann 1983)

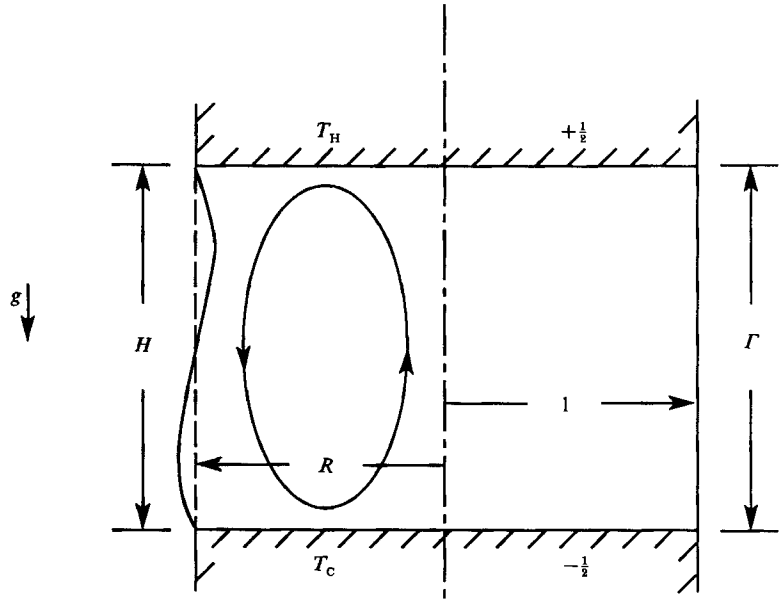

FIGURE 1. The half-zone, showing geometric and thermal conditions, both in dimensional and dimensionless forms.

is actually responsible for the appearance of these striations. Since this mode of convection will exist in any gravitational environment, the stability properties of thermocapillary convection are of possible technological importance; the identification of a region in an appropriate parameter space which is free of oscillatory thermocapillary convection is particularly relevant.

The flow domain of an actual float zone is very complicated. It is bounded by non-planar melting and freezing solid–liquid interfaces and a deformable free surface, all of which are influenced by the translation of the material through the heater. Forced convection, due to independent rotation of the feed/seed material which is utilized to reduce asymmetry in the external heating, may be present. Model experiments, however, have been designed to eliminate several of the features in an actual float zone (i.e. translation, rotation, and melting/freezing interfaces) and to minimize the influence of buoyancy relative to thermocapillarity. These experiments show that, under certain critical conditions, steady thermocapillary convection undergoes an abrupt transition to an unsteady, oscillatory-flow state. Hence, understanding of such a transition in an actual float zone may be furthered by first studying its occurrence in this simpler situation.

A schematic of one of these so-called *half-zone* experiments is shown in figure 1. Two coaxial cylindrical rods of radius R with planar ends are oriented a distance H apart with their axes in the direction of gravity. A liquid zone is created between the ends and the rods are heated differentially, with the upper rod being at a higher temperature (T_H) than the lower (T_C). Since the imposed axial temperature gradient within the liquid is vertically upward (and the radial temperature gradients are small) the half-zone is stably stratified from the standpoint of buoyancy. However, the temperature gradient which exists along the free surface causes motion along the free surface from the hot cylinder to the cold one, thereby driving bulk thermocapillary convection with the sense of circulation shown in the figure. The

flow and temperature properties of the half-zone are meant to approximate the situation in the lower half of an actual float-zone melt.

Several experiments of this variety have been performed, both in full $(1-g)$ gravity and microgravity environments. We shall mention only a few of these for the purpose of motivating further discussion. Chun (1980) performed experiments using zones of silicone oils and octadecane ($C_{18}H_{38}$) which were 3 mm in diameter and of various aspect ratios ($\Gamma \equiv H/R$). Temperatures were monitored at two locations near the free surface at opposite sides of the zone. As the temperature difference $T_H - T_C$ across the zone was increased, two modes of oscillatory thermocapillary convection were observed, depending on the value of T; for $\Gamma < 0.9$, an axisymmetric mode of oscillation was observed while for larger aspect ratios, the oscillation was non-axisymmetric. Preisser *et al.* (1983) performed similar experiments using half-zones of sodium nitrate ($NaNO_3$), monitoring the temperature oscillations occurring within the zone. Only non-axisymmetric oscillatory convection (determined by means of flow visualization) was reported. Kamotani, Ostrach & Vargas (1984) used hexadecane and Fluorinert FC-43 with an aspect-ratio range of $0.2 < \Gamma < 2$ and also report only non-axisymmetric oscillatory convection. However, recent experimental results (D. Schwabe, private communication) indicate that axisymmetric oscillatory convection *is* possible in certain regions of aspect-ratio/Prandtl-number space. Kamotani *et al.* also stress the importance of free-surface deformation to the mechanism they postulate to be responsible for the occurrence of oscillations. The onset of oscillatory thermocapillary convection has also been observed (e.g. Schwabe, Preisser & Scharmann 1982) in experiments performed in a microgravity environment, underscoring its potential effects on crystal growth in space.

One of the problems associated with model experiments is the inability to model all of the parameters relevant to an actual float zone. Perhaps the most significant example is the Prandtl number $Pr \equiv \nu/\kappa$, where ν and κ are the kinematic viscosity and thermal diffusivity, respectively. Prandtl numbers for materials grown by the float-zone process are $O(10^{-2})$ while those for the fluids typically used in model experiments are $O(10)$. The principal reason for this is that crystal-growth melts are optically opaque, while transparent fluids are desired for model experiments so that flow visualization can be employed. Another problem associated with laboratory experiments is the degree of uncertainty in the material properties themselves. One of these in particular, the rate of change of surface tension with respect to temperature (used in the construction of the dimensionless Marangoni number), is not known to a high degree of accuracy for most materials.

There has been a large amount of analytical and numerical work on various aspects of thermocapillary convection. Sen & Davis (1982) employed asymptotic methods to compute steady thermocapillary convection in a two-dimensional slot with vanishing depth-to-width (aspect) ratio, while Zebib, Homsy & Meiburg (1985) calculated numerical solutions for the two-dimensional problem with unit aspect ratio. Likewise, thermocapillary and/or forced convection in a cylindrical geometry have been treated analytically by Xu & Davis (1983), Smith (1986*a*) and Kuhlmann (1989) and numerically by Chang & Wilcox (1976), Clark & Wilcox (1980) and Fu & Ostrach (1985).

In the language of stability theory, the above work provides examples of what are called *basic states*. There has been some research on the linear stability of a few of these basic states (Smith & Davis 1983*a*, *b*; Xu & Davis 1984, 1985; Smith 1986*a*, *b*) which has identified a variety of instability mechanisms and the appropriate associated parameter spaces.

Unlike linear stability theory, energy-stability theory provides a sufficient condition for stability of a given basic state to disturbances of arbitrary amplitude. Previous applications of energy-stability theory have been made for buoyancy and Marangoni convection. Davis (1969) used energy-stability theory to analyse buoyancy and surface-tension-driven flow instabilities for non-deforming free surfaces. A comparison of the optimal stability limit with previous linear and nonlinear results showed that they are in reasonable agreement, indicating that energy-stability theory does yield results of practical utility for this case. Davis & Homsy (1980) extended this theory to problems with deformable free surfaces and found that surface deflection is stabilizing.

In order to gain further understanding of the stability properties of thermocapillary convection in a cylindrical geometry, we have chosen to model the half-zone examined experimentally by others. The previous work of Xu & Davis (1983, 1984, 1985) modelled the half-zone as having an infinite aspect ratio so that the basic-state velocity and temperature profiles in the core region of the zone could be described analytically. The results obtained using linear stability theory gave sufficient conditions for instability (in terms of a Marangoni number) which are nearly two orders of magnitude below those obtained experimentally. Once reason speculated by Xu & Davis for this discrepancy was their assumption of infinite zone length, a finite-length zone being susceptible to a smaller class of disturbances. In the hope of obtaining results which are in better agreement with the model experiments, we compute the basic state for a finite-length zone using numerical (finite-difference) methods. The basic-state velocity and temperature fields are therefore two-dimensional, rather than one-dimensional as in the work of Xu & Davis. This means that the subsequent stability problem will be governed by partial-differential equations, rather than by ordinary differential equations.

We also choose to employ energy-stability theory rather than linear stability theory for our first analysis of this basic state under the rationale that the identification of regions of stability can be of possible technological importance. If the crystal grower is able to adjust the process to stay below this limit, then it may be possible to grow striation-free material. An unconventional approach is used in the application of energy theory to our numerically determined basic state; rather than solving an eigenvalue problem defined by the Euler–Lagrange equations (corresponding to the standard variational problem), we shall attack the variational problem more directly by finite-difference discretization of the functional which appears.

The basic-state computation is outlined in §2, and the stability analysis and results are presented in §3 and §4. Comparison with available experimental results for model half-zones shows that the energy-theory results for axisymmetric disturbances do not appear to be overly conservative (small).

2. Basic state

The basic state of interest is one of swirl-free thermocapillary convection in a model half-zone of $O(1)$ aspect ratio. The flow and temperature fields are two-dimensional and must therefore be obtained numerically for the nonlinear cases of interest.

We model the liquid zone as a Newtonian, Boussinesq fluid and choose scales for length, velocity and pressure to be R, $\gamma(T_{\mathrm{H}}-T_{\mathrm{C}})/\mu$, and $\gamma(T_{\mathrm{H}}-T_{\mathrm{C}})/R$, respectively.

The quantity μ is the dynamic viscosity coefficient and $\gamma > 0$ is the rate of decrease of surface tension σ with temperature as defined by

$$\sigma = \sigma_{\mathrm{m}} - \gamma(T - T_{\mathrm{m}}),$$

where $T_{\mathrm{m}} = \frac{1}{2}(T_{\mathrm{H}} + T_{\mathrm{C}})$ is the mean temperature of the two solid cylinders and σ_{m} is the surface tension at temperature T_{m}. The velocity scale is the Marangoni velocity (Sen & Davis 1982) obtained by balancing the surface-tension gradient along the interface with the jump in shear stress. A dimensionless temperature is defined by

$$\Theta \equiv \frac{T - T_{\mathrm{m}}}{T_{\mathrm{H}} - T_{\mathrm{C}}}.$$

The resulting dimensionless governing equations for the basic-state velocity $\boldsymbol{U} \equiv (U, 0, W)$, pressure P and temperature fields are

$$\frac{1}{r}(rU)_r + W_z = 0, \tag{2.1}$$

$$Re\,(UU_r + WU_z) = -P_r + \nabla^2 U - \frac{U}{r^2}, \tag{2.2}$$

$$Re\,(UW_r + WW_z) = -P_z + \nabla^2 W + \frac{Gr}{Re}\Theta, \tag{2.3}$$

$$Ma\,(U\Theta_r + W\Theta_z) = \nabla^2 \Theta, \tag{2.4}$$

where

$$\nabla^2 \equiv \frac{1}{r}\frac{\partial}{\partial r}\left(r\frac{\partial}{\partial r}\right) + \frac{\partial^2}{\partial z^2}.$$

The three dimensionless parameters which appear are:

Reynolds number $$Re = \frac{\gamma(T_{\mathrm{H}} - T_{\mathrm{C}})R}{\mu\nu},$$

Grashof number $$Gr = \frac{g\alpha(T_{\mathrm{H}} - T_{\mathrm{C}})R^3}{\nu^2},$$

Marangoni number $$Ma = \frac{\gamma(T_{\mathrm{H}} - T_{\mathrm{C}})R}{\mu\kappa},$$

where g is the gravitational acceleration, α is the coefficient of volumetric expansion and the conventional subscript notation has been used to denote partial differentiation. The Prandtl number is obtained from the quotient Ma/Re.

We assume, as a first approximation, that the free surface is not permitted to deform, and so is fixed at $r = 1$. This corresponds to requiring that the volume of liquid in the half-zone is $\pi\Gamma$ and that the mean surface tension, σ_{m}, is asymptotically large. The boundary conditions applied to complete the problem specification are:

$$U = W = 0, \quad \Theta = -\tfrac{1}{2}; \quad z = 0, \tag{2.5a–c}$$

$$U = W = 0, \quad \Theta = \tfrac{1}{2}; \quad z = \Gamma, \tag{2.6a–c}$$

$$U = 0, \quad U_z + W_r = -\Theta_z, \quad -P + 2U_r = \frac{-\sigma}{\sigma_{\mathrm{m}} Ca}, \quad \Theta_r = -Bi\,[\Theta - \Theta_{\mathrm{a}}(z)]; \quad r = 1, \tag{2.7a–d}$$

$$U = W_r = \Theta_r = 0; \quad r = 0. \tag{2.8a–c}$$

Equations (2.5) and (2.6) express the kinematic and no-slip conditions and the requirement of isothermal surfaces, while (2.7*a*) is the kinematic condition on the free surface. Equations (2.7*b*, *c*) represent the shear and normal-stress balances. Symmetry conditions at the axis of symmetry are given by (2.8). The additional parameter appearing in (2.7*d*), which models the heat-transfer mechanism at the free surface, is the Biot number,

$$Bi = hR/k$$

where h is a heat-transfer coefficient and k is the thermal conductivity of the liquid. Since h may vary with z, in general, $Bi = Bi(z)$. This simple conductive mechanism for heat transfer between the liquid and the external environment (at specified temperature $\Theta_a(z)$) was adopted for consistency with the work of Xu & Davis (1983, 1984, 1985). For the majority of the calculations $\Theta_a(z) = -\frac{1}{2}$, i.e. the environment was assumed to be at a constant temperature equal to that of the cold cylinder at $z = 0$. Condition (2.7*c*) contains the capillary number

$$Ca = \frac{\gamma(T_H - T_C)}{\sigma_m}$$

which vanishes in the limit of a non-deformable free surface. Hence, this condition is not required in the present analysis.

The numerical solution of this problem is accomplished by first transforming to a stream-function/vorticity form, thereby eliminating the pressure. The stream function Ψ and the vorticity ζ are defined by

$$U = \frac{1}{r}\Psi_z, \quad W = -\frac{1}{r}\Psi_r, \quad \zeta = U_z - W_r,$$

and the problem to be solved transforms to

$$\nabla^2\Psi - \frac{2}{r}\Psi_r = r\zeta, \tag{2.9}$$

$$Re\left(-\frac{\zeta}{r^2}\Psi_z + \frac{1}{r}\Psi_z\zeta_r - \frac{1}{r}\Psi_r\zeta_z\right) = \nabla^2\zeta - \frac{\zeta}{r^2} - \frac{Gr}{Re}\Theta_r, \tag{2.10}$$

$$Ma\left(\frac{1}{r}\Psi_z\Theta_r - \frac{1}{r}\Psi_r\Theta_z\right) = \nabla^2\Theta, \tag{2.11}$$

with boundary conditions

$$\Psi = 0, \quad \zeta = \frac{1}{r}\Psi_{zz}, \quad \Theta = \mp\tfrac{1}{2}; \quad z = 0, \Gamma, \tag{2.12a–f}$$

$$\Psi = \zeta = \Theta_r = 0; \quad r = 0, \tag{2.13a–c}$$

$$\Psi = 0, \quad \zeta = \Theta_z, \quad \Theta_r = -Bi[\Theta - \Theta_a(z)]; \quad r = 1. \tag{2.14a–c}$$

These equations are solved using a modification of the predictor-corrector multiple iteration (PCMI) technique employed successfully by Neitzel & Davis (1981) and Neitzel (1984) to study centrifugally unstable flows in cylindrical geometries; the reader is referred to these papers for details. The modification consists of the addition of the energy equation (2.11) and replacement of the time-stepping (since we are computing a steady solution) by an outer-iteration loop for solving the vorticity equation (2.10). The energy (2.11) and stream function (2.9) equations are solved in an inner loop by successive line over-relaxation (SLOR). Mesh stretching is employed in the radial direction when necessary to resolve steep gradients which can exist there.

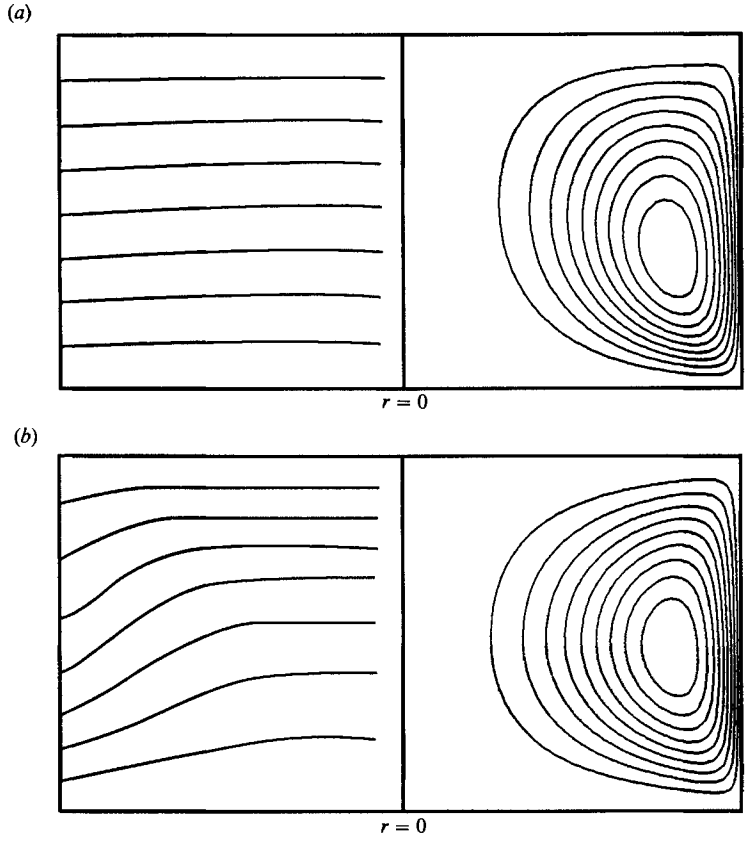

FIGURE 2. Basic-state isotherms and streamlines for $\Gamma = 1$, $Ma = 100$, $Gr = 0$, $Bi = 0.3$ and $\Theta_a(z) = z - \frac{1}{2}$. (*a*) $Pr = 0.01$, (*b*) $Pr = 10$.

Convergence is achieved for the inner loop in typically less than 25 iterations for a relative error of 10^{-4}. For the outer loop, anywhere from 20 to 2800 iterations can be required, depending on the parameters of the problem and the mesh employed. The CPU time required to calculate a typical basic state on an IBM 3090 computer for a 41×41 mesh using double-precision arithmetic is roughly 20 s.

States of steady thermocapillary convection were computed for a variety of parameters to check the validity of the results before proceeding with a stability analysis. Available for comparison were the numerical results of Fu & Ostrach (1985), the analytical solution of Xu & Davis (1983) for very long zones and recent analytical, two-dimensional solutions of Kuhlmann (1989) valid for circumstances in which the flow in the half-zone possesses symmetry about the midplane $z = \frac{1}{2}$. In all cases, the comparison is favourable and it is felt that the basic state is being computed faithfully.

All computed half-zone flows consist of a single toroidal cell with flow at the surface in the direction opposite to that of the surface-temperature gradient, as expected. As previously mentioned, one of the difficulties associated with extrapolation of the results of model experiments to cases of interest to crystal growers is the fact that the Prandtl number is different by a couple of orders of magnitude in the two situations. A case with moderate Marangoni number and exterior environment temperature which is linear in z is shown in figure 2; in figure

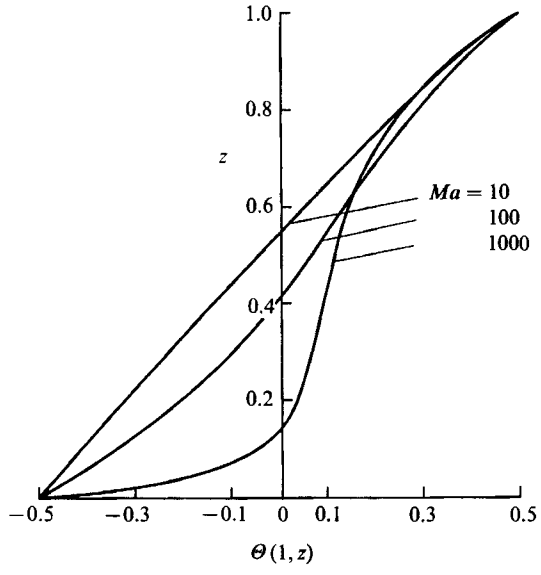

FIGURE 3. Free-surface temperature profiles for $\Gamma = 1$, $Pr = 1$, $Gr = 0$, $Bi = 0.3$ and $\Theta_a(z) = -\frac{1}{2}$.

2(*a*), $Pr = 0.01$, while in figure 2(*b*), $Pr = 10$. These Prandtl numbers are roughly representative of molten silicon and sodium nitrate (the material used in the model experiments of Preisser *et al.* 1983), respectively. The distortion, at high Pr, of the isotherms from the nearly conductive low-Pr state and shift in the centre of the eddy are clearly evident in the figure.

Also of interest is the effect of Marangoni number on the free-surface temperature profile, since it is the surface-temperature gradient which serves as the driving force for the flow. This is shown in figure 3 for a case with unit Prandtl number and cold-wall exterior temperature. As Ma increases, the more vigorous motion which results causes this profile to depart from the nearly linear form it has at lower Marangoni numbers; the temperature gradient in the vicinity of the cold wall becomes particularly steep and the profile begins to become S-shaped (Kamotani *et al.* 1984). It has been conjectured by Kamotani *et al.* that the occurrence of such a surface-temperature profile is responsible for the onset of oscillatory thermocapillary convection.

3. Energy-stability analysis

We begin the energy-theory analysis of the basic state in the usual fashion by deriving the energy identity. We assume there exists a solution $[\boldsymbol{u}, p, T]$ to the governing equations ((2.1), plus the unsteady analogue of (2.2)–(2.4)) which is an axisymmetric perturbation to the axisymmetric basic state, i.e.

$$[\boldsymbol{u}, p, T] = [U(r,z), 0, W(r,z), P(r,z), \Theta(r,z)] + [u'(r,z,t), 0, w'(r,z,t), p'(r,z,t), T'(r,z,t)]. \quad (3.1)$$

While the assumption of axisymmetric disturbances may limit the applicability of the results, available experimental evidence indicates that such an assumption is relevant for certain values of some of the parameters. Hopefully, the results of this

analysis, when coupled with subsequent results for three-dimensional disturbances, will identify these values. It is also hoped, on the basis of linear-theory results of Xu & Davis (1984), that the stability limits for axisymmetric and non-axisymmetric disturbances will not differ to a great degree. In any event, at the present time, available computer resources are insufficient to support the computational effort necessary to deal with this general case.

Substitution of (3.1) into the governing equations and boundary conditions leads to a system of equations for the disturbance quantities. We then take the inner product of the disturbance momentum equation with $\boldsymbol{u}'$, add to this the disturbance energy equation multiplied by $\lambda PrT'$, and integrate over the volume

$$V = \{(r,\theta,z)|0 \leqslant r \leqslant 1, 0 \leqslant \theta \leqslant 2\pi, 0 \leqslant z \leqslant \Gamma\}$$

occupied by the liquid, using the disturbance boundary conditions. The result is the exact disturbance-energy evolution equation

$$\frac{\mathrm{d}E}{\mathrm{d}t} = -PrD - MaI + PrJ, \tag{3.2}$$

where

$$E = \frac{1}{2}\int_V (\boldsymbol{u}'\cdot\boldsymbol{u}' + \lambda Pr\, T'^2)\,\mathrm{d}V,$$

$$I = \int_V \left(\boldsymbol{u}'\cdot\boldsymbol{D}\cdot\boldsymbol{u}' + \lambda Pr\, T'\nabla\Theta\cdot\boldsymbol{u}' - \frac{Gr}{Re^2}w'T'\right)\mathrm{d}V,$$

$$D = \int_V (\nabla\boldsymbol{u}' : \nabla\boldsymbol{u}' + \lambda\nabla T'\cdot\nabla T')\,\mathrm{d}V,$$

$$J = \int_S (-w'T'_z - \lambda Bi\, T'^2)\,\mathrm{d}S$$

and S is the free surface $r = 1$. The velocity and temperature disturbances have been joined by a positive *coupling parameter* λ (Joseph 1976) to form a generalized disturbance energy, E, and the quantity $\boldsymbol{D}$ in the production integral I is the symmetric basic-state deformation-rate tensor,

$$\boldsymbol{D} = \begin{bmatrix} U_r & 0 & \frac{1}{2}(U_z + W_r) \\ & U/r & 0 \\ & & W_z \end{bmatrix}.$$

Employing the reformulated energy theory of Davis & von Kerczek (1973), (3.2) is divided by the positive-definite functional E and an upper bound is constructed for the resulting right-hand side, viz.

$$\frac{1}{E}\frac{\mathrm{d}E}{\mathrm{d}t} = \frac{1}{E}(-PrD - MaI + PrJ) \leqslant \nu = \max_H\left(\frac{-PrD - MaI + PrJ}{E}\right), \tag{3.3}$$

where the maximum is taken over the space of kinematically admissible functions,

$$H = \{\boldsymbol{u}', T' \,|\, \boldsymbol{u}' = T' = 0 \text{ at } z = 0, \Gamma; \boldsymbol{u}' = 0 \text{ at } r = 0, 1; \nabla\cdot\boldsymbol{u}' = 0\}.$$

We choose to formulate the problem so that the Marangoni number is the stability parameter. For fixed values of the other parameters associated with the problem, the smallest value of Ma that corresponds to the condition $\nu = 0$ will be called $Ma^*(\lambda)$.

Since λ is a free parameter, the maximum value of Ma^* for positive values of λ is sought (Joseph 1976). In the general case of three-dimensional disturbances, this

value would be the energy-stability limit, Ma_E, i.e. the flow would be asymptotically stable in the mean for $Ma < Ma_E$. Since we have restricted attention to two-dimensional disturbances, this value is, at worst, an upper bound to Ma_E. With this restriction in mind, we shall use the notation Ma_E to refer to the value obtained from the present analysis,

$$Ma_E = \max_{\lambda > 0} Ma^*. \tag{3.4}$$

In many analyses, the search for this maximum is not performed. Rather, the variable λ is arbitrarily set to some value, say $\lambda = 1$, and the result is accepted as a lower bound to the actual energy-stability limit. It will be seen that, for the problem of interest here, the effort necessary to determine Ma_E is extremely worthwhile.

3.1. *Formulation of the discrete problem*

Typically, Ma^* is calculated by treating the Euler–Lagrange system which arises from the maximum problem in (3.3). However, this approach is not practical here since the two-dimensional variation of the basic state prohibits the use of the standard normal-mode analysis to reduce this system of partial-differential equations to ordinary differential equations. Moreover, in the present problem, the basic state, which appears in the coefficients of these equations, is known only numerically. Thus, we choose to approach the calculation of Ma^* by directly treating the functional ν in (3.3).

It is convenient to consider a slightly different functional which incorporates the divergence constraint by means of a Lagrange multiplier. Hence, the maximum problem to be solved is expressed as

$$\max_{h} \left[-PrD - MaI + PrJ + 2\int_V \pi \nabla \cdot \boldsymbol{u}' \, \mathrm{d}V + \bar{\nu}(E-1) \right] = 0, \tag{3.5}$$

where $\bar{\nu}$ is a Lagrange multiplier expressing the arbitrary normalization $E = 1$, $\pi(r, z)$ is a Lagrange multiplier, and h is the extension of H obtained by removing the divergence constraint. It is easy to show that $\bar{\nu} = \nu$. Thus, since the stability condition is given by $\nu = 0$, we are interested in the variation of the quadratic functional

$$F = -PrD - MaI + PrJ + 2\int_V \pi \nabla \cdot \boldsymbol{u}' \, \mathrm{d}V.$$

A discrete version of this functional follows in an obvious way. A grid system, which divides the flow region into N rectangular subdomains, is chosen. The unknown values of the disturbance velocity and temperature at the intersections of the grid are denoted by $u_{i,j}$, $w_{i,j}$ and $T_{i,j}$. Since the Lagrange multiplier π plays the same role as the fluid pressure, a staggered grid is employed for it (see figure 8 in the Appendix); the unknown values of π at the intersections of its grid are denoted by $\pi_{k,l}$. The various derivatives in the integrals of F are replaced by finite differences. The integrals are approximated on each subdomain by finite summations using the disturbance boundary conditions, where applicable, and finally the discrete version of the functional, F_D, is formed by summing over all N subdomains:

$$F_D = -Pr \sum_{i=1}^{N} \left[\left(\frac{\Delta u}{\Delta r}\right)_i^2 + \left(\frac{\Delta u}{\Delta z}\right)_i^2 + \left(\frac{u_i}{r}\right)^2 + \left(\frac{\Delta w}{\Delta r}\right)_i^2 + \left(\frac{\Delta w}{\Delta z}\right)_i^2 + \left(\frac{\Delta \phi}{\Delta r}\right)_i^2 + \left(\frac{\Delta \phi}{\Delta z}\right)_i^2 \right] r_i \, \Delta r \, \Delta z$$
$$- Ma \sum_{i=1}^{N} \left[u_i^2 D_{11} + 2u_i w_i D_{13} + w_i^2 D_{33} \right.$$

$$+u_i\phi_i Pr\lambda^{\frac{1}{2}}\frac{\partial\Theta}{\partial r}+w_i\phi_i\left(Pr\lambda^{\frac{1}{2}}\frac{\partial\Theta}{\partial z}-\frac{Gr}{Re^2\lambda^{\frac{1}{2}}}\right)\Bigg]r_i\Delta r\Delta z$$

$$+Pr\sum_{j=1}^{K}\left[-\frac{1}{\lambda^{\frac{1}{2}}}w_j\left(\frac{\Delta\phi}{\Delta z}\right)_j\right]\Delta z$$

$$-Pr\sum_{j=1}^{K}Bi\,\phi_j^2\Delta z+2\sum_{i=1}^{N}\pi_i\left[\left(\frac{\Delta u}{\Delta r}\right)_i+\frac{u_i}{r}+\left(\frac{\Delta w}{\Delta z}\right)_i\right]r_i\Delta r\Delta z. \tag{3.6}$$

D_{ij} is the (i,j)th element of $\boldsymbol{D}$, T has been replaced by $\phi/\lambda^{\frac{1}{2}}$ for convenience, K is the number of subintervals in the surface integral and $(\Delta/\Delta z)_i$, and $(\Delta/\Delta r)_i$ are finite-difference expressions for derivatives in the z- and r-directions, respectively. A single subscript in (3.6) refers to the average value of the respective dependent variable for the indicated domain of integration. Details of this process are provided in the Appendix.

A stationary value of F_{D} is located by differentiating it with respect to each unknown and setting each of these derivatives to zero, i.e.

$$\frac{\partial F_{\mathrm{D}}}{\partial q_n}=0, \quad q_n=u_{i,j}, w_{i,j}, \phi_{i,j} \quad \text{or} \quad \pi_{k,l}. \tag{3.7}$$

This process yields a generalized algebraic eigenvalue problem. We seek the minimum positive eigenvalue of this system as the approximate (subject to discretization error) value of Ma^*. Calling the vector consisting of the unknowns on all grid points $\boldsymbol{X}$, we rewrite (3.7) in the matrix form

$$\boldsymbol{A}\boldsymbol{X}=\rho\boldsymbol{B}(Ma)\,\boldsymbol{X}, \tag{3.8}$$

where $\boldsymbol{A}$ and $\boldsymbol{B}$ are indefinite, symmetric matrices with $\boldsymbol{A}$ having a banded structure and $\boldsymbol{B}$ depending on the basic-state deformation-rate tensor $\boldsymbol{D}$. The symmetry of the discrete problem is consistent with that of the variational problem (3.5). Other discretizations were tried which did not preserve this symmetry and were therefore discarded. The dependence on the basic state, which depends in turn on the Marangoni number Ma, complicates the calculation of Ma^* (Munson & Joseph 1971). For a given value of Ma, denote the smallest positive eigenvalue of the generalized eigenvalue problem (3.8) by ρ^*. If $\rho^* \neq Ma$, then a new Ma is chosen, the basic state recomputed, and the eigenvalues recalculated. This process is repeated until $\rho^* = Ma$, in which case, $Ma^* = \rho^*$. This, of course, assumes all other parameters, including the coupling parameter λ, are fixed, necessitating further computation to find Ma_E according to (3.4). The numerical problem associated with these eigenvalue computations is, like the approach to the stability problem, somewhat unconventional. For this reason, the procedure by which ρ^* and Ma_E are computed is described in some detail below.

3.2. *Numerical procedure for finding* Ma_E

Equation (3.8) represents a nonlinear generalized eigenvalue problem. The matrices $\boldsymbol{A}$ and $\boldsymbol{B}$ are symmetric and sparse, but, in general, indefinite. In addition to the basic-state dependence of $\boldsymbol{B}$ mentioned above, $\boldsymbol{A}$ and $\boldsymbol{B}$ depend on the other parameters of the problem, namely Pr, Gr and the coupling parameter, λ. We first address the case that all these parameter are fixed, reducing (3.8) to the generalized eigenvalue problem

$$\boldsymbol{A}\boldsymbol{X}=\rho\boldsymbol{B}\boldsymbol{X}, \quad \|\boldsymbol{X}\|=1, \tag{3.9}$$

where $\|\cdot\|$ denotes the Euclidean norm.

The eigenvalues ρ of (3.9) may be real of either sign or be complex-conjugate pairs. To each null vector of $\boldsymbol{B}$ corresponds an 'infinite' eigenvalue (at least N of these are known to occur), while the null vectors of $\boldsymbol{A}$ yield zero eigenvalues. Standard linear-algebra software packages provide implementations of the QZ-algorithm for eigenvalue problems of the form (3.9). These packages compute all of the eigenvalues of the system (our stability result requires only a single eigenvalue), do not exploit the sparseness of $\boldsymbol{A}$ and $\boldsymbol{B}$ and are therefore suitable only for relatively coarse discretizations of the underlying continuous problem. The method adopted for the present computations makes use of both the symmetry and sparseness of $\boldsymbol{A}$ and $\boldsymbol{B}$ and computes only the eigenvalue of interest – the smallest, positive one.

The algorithm of choice for finding a single eigenvalue of (3.9) appears to be some form of *inverse iteration*. The technique used here is a generalization of that employed by Bank & Mittelmann (1986) for the simpler problem of finding the smallest eigenvalue of a positive-definite matrix. For this a starting vector $\boldsymbol{X}_0$, $\|\boldsymbol{X}_0\| = 1$, is needed. Initially, this inverse-iteration process is started with a random vector. Subsequent iterations use previously computed eigenvectors corresponding to nearby parameter values. A first approximation for ρ is obtained through the *Rayleigh quotient*

$$\rho_0 = \boldsymbol{X}_0^{\mathrm{T}} \boldsymbol{A} \boldsymbol{X} / \boldsymbol{X}_0^{\mathrm{T}} \boldsymbol{B} \boldsymbol{X}_0. \tag{3.10}$$

In the unlikely event that the denominator is zero, a different $\boldsymbol{X}_0$ has to be chosen.

Given this initial pair $\boldsymbol{X}_0$ and ρ_0, the inverse-iteration procedure is performed as follows:

1. Solve $(\boldsymbol{A} - s\boldsymbol{B})\,\bar{\boldsymbol{Y}} = (\rho_k \boldsymbol{B} - \boldsymbol{A})\,\boldsymbol{X}_k$ and define $\boldsymbol{Y} = (\bar{\boldsymbol{Y}} - \boldsymbol{X}_k \bar{\boldsymbol{Y}}^{\mathrm{T}} \boldsymbol{X}_k)/\|\bar{\boldsymbol{Y}} - \boldsymbol{X}_k \bar{\boldsymbol{Y}}^{\mathrm{T}} \boldsymbol{X}_k\|$.
2. Form $\boldsymbol{Q} = [\boldsymbol{X}_k | \boldsymbol{Y}]$ and solve the 2×2 problem

$$\boldsymbol{Q}^{\mathrm{T}} \boldsymbol{A} \boldsymbol{Q} \boldsymbol{Z} = \tau \boldsymbol{Q}^{\mathrm{T}} \boldsymbol{B} \boldsymbol{Q} \boldsymbol{Z}$$

for the eigenvalues τ_1, τ_2 and associated normalized eigenvectors $\boldsymbol{Z}_1$, $\boldsymbol{Z}_2$. Without loss of generality let τ_1 be the smallest positive eigenvalue.

3. Set $\rho_{k+1} = \tau_1$, $\boldsymbol{X}_{k+1} = \boldsymbol{Q}\boldsymbol{Z}_1$ and check for convergence. If not converged, increment iteration index k and repeat.

Several remarks are in order on the above algorithm. The quantity s is a positive real number which has to be closer to the desired eigenvalue than to any of the other eigenvalues. While, in some applications this 'shift parameter' may have to be adjusted during the computation in order to satisfy this requirement, this was not necessary in the present case. Earlier computations with the QZ-algorithm for moderate-size problems had shown that, for the cases considered, there were no complex-conjugate pairs that were smaller in modulus than ρ^*. Also, the negative eigenvalue of smallest modulus was similar in modulus to ρ^*. It was thus relatively easy, with some rough knowledge of ρ^*, to find a value for s.

The eigenvalue problem in step 2 is basically an orthogonal projection of the original problem into the subspace spanned by the columns of Q_k. Simpler inverse-iteration algorithms are indeed available; however, their application to the present problem did not yield satisfactory results. In general, of course, this 2×2 eigenvalue problem may have complex eigenvalues, as well as real ones. While several precautions for this and other cases were put into the program, they will not be described here, being a rather technical detail. Eventually τ_1 will be positive and approximate ρ^* while $\boldsymbol{Q}\boldsymbol{Z}_1$ approximates the associated eigenvector. The quantities $\boldsymbol{X}_{k+1}$ and ρ_{k+1} are related through the Rayleigh quotient (3.10).

While steps 2 and 3 need no further explanation, the solution of the linear system

in step 1 represents a non-trivial problem. The matrix on the left is symmetric but indefinite. The newest version of the FORTRAN subroutine SYMMLQ, part of the NAG library, was used. It applies a conjugate-gradient method and permits preconditioning by a positive-definite matrix. No attempt was made to find a near-optimal choice for the preconditioner. In all computations it was taken as the diagonal matrix with the ith element equal to the Euclidean norm of the ith column of the matrix $\boldsymbol{A}-s\boldsymbol{B}$.

The convergence of the above inverse-iteration procedure is linear with a factor asymptotically equal to

$$\left|\frac{s-\rho^*}{s-\rho_n}\right| < 1,$$

where ρ_n is the next nearest eigenvalue of (3.9) to s. Choosing s close to ρ^* will thus speed up convergence of the inverse iteration while, in general, requiring more conjugate-gradient iterations for the nearly singular system matrix. The essential computational requirement per conjugate-gradient iteration is one matrix-vector multiplication with the system matrix.

In addition to this method for solving the eigenvalue problem, two outer iterations are needed to determine the energy-stability limit Ma_E. The requirement that $\rho^*(Ma) = Ma$ suggests a fixed-point iteration. The second requirement, that Ma_E is found as the maximum of all these ρ^* with respect to λ, suggests an optimization procedure. No attempt was made to simultaneously attack both these problems. Both possibilities of a successive solution were used, the fixed-point iteration as either an inner or outer iteration. In the first case, say, when λ is temporarily fixed, the following would be the well-known Picard iteration

$$\boldsymbol{A}\boldsymbol{X}_{k+1} = \rho_{k+1}\boldsymbol{B}(\rho_k)\,\boldsymbol{X}_{k+1}, \quad k = 0, 1, 2, \ldots, \tag{3.11}$$

where ρ_{k+1}, $\boldsymbol{X}_{k+1}$ is the solution found through the inverse-iteration procedure defined above. This iteration will only converge if $|\varphi'(Ma^*)| < 1$, where φ denotes the relationship between ρ_{k+1} and ρ_k given through (3.11) and if started close enough to Ma^*. A simple acceleration procedure due to Aitken (1926) was implemented to guarantee convergence:

$$\left.\begin{aligned} \rho_k^{(0)} &= \rho_k, \quad \rho_k^{(i)} = \varphi(\rho_k^{(i-1)}), \quad i = 1, 2, \\ \rho_{k+1} &= \rho_k + \frac{(\rho_k^{(1)} - \rho_k^{(0)})^2}{(\rho_k^{(1)} - \rho_k^{(0)}) - (\rho_k^{(2)} - \rho_k^{(1)})}. \end{aligned}\right\} \tag{3.12}$$

The sequence $\{\rho_k\}$ converges quadratically if φ is twice continuously differentiable and $\varphi'(Ma^*) \neq 1$.

For completeness we also outline how the maximization of Ma^* with respect to λ was accomplished. Starting from an initial value λ_1 and corresponding value ρ_1 (or Ma_1) two additional pairs of values are computed with their λ-values in the vicinity of λ_1. Through these three points a quadratic parabola is fitted and the point corresponding to its maximum replaces one of the points. The parabola need not have a maximum; in the event that a minimum occurs, some modification is required. The details will again not be given here since they are straightforward. As is well known, maximization through successive quadratic interpolation has a convergence order of about 1.3.

The iterative procedure described above provides a relatively efficient method to calculate Ma_E. After computation of the first basic state, subsequent basic-state computations need fewer relaxations if they are done for a convergent sequence of

Marangoni numbers. Analogously, the inverse iteration only requires several (more than 1–2) iterations when initiated, i.e. with the random vector $\boldsymbol{X}_0$. It is thus not surprising that the entire computation of Ma_E took only a few times the amount of work needed for the first basic state and ρ^*-computation. It should be noted that, to minimize inaccuracies introduced by differentiation of basic-state quantities, the basic state was computed on a grid with twice the resolution used for the stability calculations.

3.3 *Code verification*

Because of the complex nature of the half-zone problem and the unconventional approach employed to obtain energy-stability limits for this basic state, another related problem was sought for use in verification of the resulting computer code. The problem chosen was the stability of the static state in a fluid-filled cylinder in a body-force field heated from below. The governing dimensionless parameter for this problem is the Rayleigh number Ra; as Ra increases from zero, the static state loses stability and convection sets in. Subsequent increases in Ra cause bifurcation to other flow states, but it is this first instability with which we are concerned, since it can be shown that the energy- and linear-stability limits for this coincide. We may thus compare our energy-stability limit for this case with linear-stability limits obtained previously by Charlson & Sani (1970) and Yamaguchi, Chang & Brown (1984).

While the heated-cylinder problem has a cylindrical geometry similar to the half-zone, there are two significant differences which make it less than perfect for such a verification. First, the cylindrical surface of the heated cylinder is a rigid wall, meaning that no surface integral J appears in the energy identity analogous to (3.2). Second, the static basic state need not be computed numerically, so that the influence of inaccuracies in the basic-state solution on the stability limits cannot be observed. In spite of these reservations, there appear to be no other previously solved problems which are a better match to the problem of interest here.

Energy-stability calculations were performed for the heated-cylinder problem for both perfectly conducting and perfectly insulated cylindrical surfaces. The results ($(Ra_c)^{\frac{1}{3}} = (Ra_E)^{\frac{1}{3}} = (Ra_L)^{\frac{1}{3}}$) obtained for unit aspect ratio are presented in table 1 as a function of grid density. Initial guesses of the eigenvalues (guesses below and slightly above the final result were tried) do not alter the results shown in the table by more than ± 0.01. For both boundary conditions, agreement with the linear limits of Charlson & Sani (1970) and Yamaguchi *et al.* (1984) is excellent. Results for aspect ratios other than unity were also verified with equal success.

4. Results and discussion

The calculations of Ma_E described in §3 have been performed for a variety of parameters on both the Arizona State University IBM 3090-500E/VF supercomputer and on an Ardent Titan mini-supercomputer in the Advanced Research Computing Facility of the Department of Mathematics; the results of these are summarized in tables 2 and 3 and figures 4–6. This procedure requires maximizing the smallest positive eigenvalue Ma^* over the space of positive coupling parameters λ according to (3.4), the other parameters remaining fixed. It is seen from the data that this variation is significant, amounting to two orders of magnitude for the cases presented. As implemented, the procedure described in §3 did not iterate to find a fixed point, i.e. $\rho^*(Ma) = Ma$, for each value of λ, since this would be an inefficient use of computational facilities. However, this was done for unit aspect ratio and two

	$(Ra_c)^{\frac{1}{2}}$	
Grid	Insulated wall	Conducting wall
20×20	47.81	50.76
40×40	47.61	50.52
50×50	47.58	50.50
70×70	47.56	50.46
C & S	47.56	50.45
Y, C & B	47.64	—

TABLE 1. Calculated values of the critical Rayleigh number for the heated cylinder problem C & S – Charlson & Sani (1970); Y, C & B – Yamaguchi *et al.* (1984)

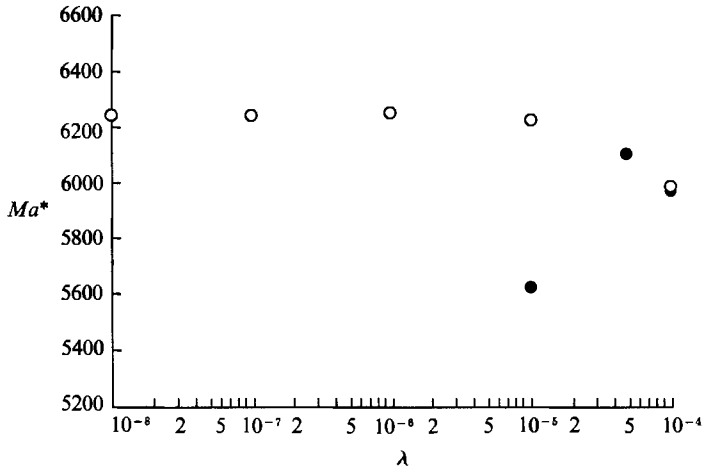

FIGURE 4. Variation of Ma^* with λ for $Pr = 1$: ○, $Gr = 0$; ●, $Gr = 1000$.

values of the Grashof number to show the behaviour of Ma^* with λ; a portion of these results is plotted in figure 4. For $Gr = 1000$, there is a clear maximum in Ma^* for $\lambda \approx 4.4 \times 10^{-5}$. For $Gr = 0$, initial computations did not use as fine a discretization as those presented here and did not consider values of λ smaller than say $O(10^{-6})$, with the result being that a maximum was not detected; in fact, it appeared that Ma^* was asymptotically approaching a maximum at $\lambda = 0$. More recent results for λ as small as 10^{-9}, however, indicate that there appears to be a maximum Ma^* occurring near 10^{-7}. Although the changes in Ma^* computed for these smaller values of λ are small, they are likely to be larger than the expected discretization error. This has been verified for the $Gr = 0$ case shown in table 2 with $\lambda = 10^{-7}$. Computations with grids of 40×38, 50×48 and 60×58 yielded values of Ma^* of 6447, 6451, and 6312, respectively, compared to 6302 obtained with a 70×68 grid. From the data in table 2, one can see that Ma^* decreases quite rapidly with increasing λ as one moves away from the maximum.

Since λ provides the coupling between the velocity and thermal disturbances in the energy functional E (see definition following (3.2)), the physical meaning of such a small maximizing λ is unclear, other than to indicate, perhaps, that the nature of the instability may be more hydrodynamic than thermal. Considering for the moment the case $Gr = 0$, an examination of the discretized functional F_D (3.6) shows that,

	Ma^*	
λ	$Gr = 0$	$Gr = 10^3$
2	62.9	69.8
1	90.6	99.6
0.50	131.9	143.2
0.25	194	207.3
0.1	333	—
0.05	525	535
0.01	1565	1547
0.005	2326	2305
0.001	4492	4501
10^{-4}	6015	5998
4.4×10^{-5}	—	6082
10^{-5}	6247	5635
10^{-6}	6253	—
10^{-7}	6302	—
10^{-8}	6275	—
10^{-9}	6274	—

TABLE 2. Variation of Ma^* with λ for two values of Gr. For all cases, $\Gamma = 1$, $Pr = 1$, $Bi = 0.3$, $\Theta_a(z) = -0.5$ and a 70×68 grid was used

as $\lambda \to 0$, the term in F_D which becomes dominant is the hydrodynamic contribution to the surface integral. The two-dimensionality of the basic state, coupled with the global nature of energy-stability theory and the fact that disturbances are not necessarily dynamically admissible make detailed physical interpretation difficult. What is obvious, however, is that the order-of-magnitude variations of Ma^* with λ which are observed make the search for the maximizing λ imperative. Had we merely adopted, say Ma^* ($\lambda = 1$) as a lower bound to Ma_E, the results would have been quite conservative and of little potential use to an experimentalist.

The results given in table 3 are presented in terms of $Re_E = Ma_E/Pr$ for convenience so that all will be of the same order of magnitude. For the cases of $Gr = 0$, $Pr \neq 1$, a value of 10^{-7} is shown in the table for the coupling parameter. In these cases, a search for a maximizing λ of less than this value was not performed, based upon experience with the $Pr = 1$, $Gr = 0$ case and the weak variations of Ma^* which were observed. The results corresponding to $\lambda = 10^{-7}$ should be very close to the actual stability limits in these cases.

Of interest are the variations of the energy limit with Pr, Gr and Γ. For a fixed value of the Grashof number, Re_E (and therefore Ma_E) increases monotonically with Prandtl number. For fixed Pr, however, the variations with Grashof number are not as simple, as seen in figure 5. For $Pr = 0.1$, Re_E increases with increasing Grashof number, while for Prandtl numbers of 0.5 and 1, this trend appears to reverse. Although results could not be obtained for Prandtl numbers corresponding to those of the model experiments (see below), the behaviour of the results for larger Prandtl numbers is contrary to what might be expected on the basis of the physical argument posed by Xu & Davis (1984), namely that the density stratification of the half-zone should be stabilizing with increasing gravity. For $Pr = 0.1$, a very weak dependence of this type was indeed observed, meaning that the stability of thermocapillary convection in half-zones of such liquids cannot be guaranteed for as large a Marangoni number in a microgravity environment as it can on Earth. Of course,

Γ	Pr	Gr	Re_E	λ	Grid
1	0.01	0	2595	10^{-7}	70×68
—	0.05	—	2996	—	—
—	0.10	—	3689	—	—
—	0.50	—	5488	—	—
—	1.0	—	6302	—	—
—	1.1	—	6430	—	—
—	1.2	—	6578	—	—
—	1.3	—	6701	—	—
—	1.4	—	6914	—	—
—	1.5	—	7017	—	—
—	1.6	—	7170	—	—
—	0.005	500	3011	1.1×10^{-3}	—
—	0.005	1000	3023	2.2×10^{-2}	—
—	0.1	500	3708	3.7×10^{-4}	—
—	0.1	1000	3734	7.3×10^{-4}	—
—	0.5	500	5397	5.4×10^{-5}	—
—	0.5	1000	5462	9.8×10^{-5}	—
—	1.0	500	6163	2.1×10^{-5}	—
—	1.0	1000	6082	4.4×10^{-5}	—
0.5	0.1	0	6719	10^{-7}	99×48
0.5	1.0	—	10799	—	99×48
0.67	0.1	—	4985	—	76×49
0.67	1.0	—	8249	—	76×49
1.33	0.1	—	2110	—	55×71
1.33	1.0	—	4509	—	55×71
2.0	0.1	—	1363	—	50×97
2.0	1.0	—	3601	—	50×97

TABLE 3. Energy-stability results for axisymmetric disturbances. For all cases, $Bi = 0.3$ and $\Theta_a(z) = -0.5$

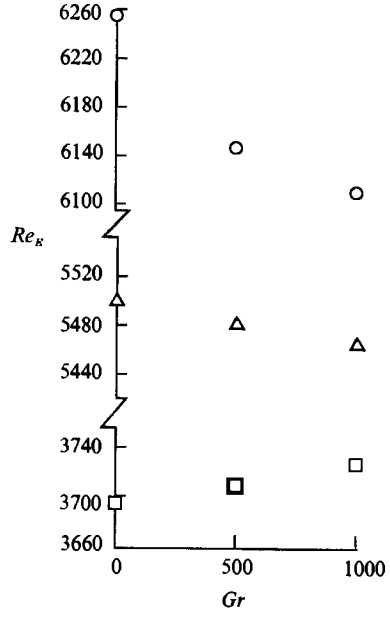

FIGURE 5. Variation of Re_E with Gr: ○, $Pr = 1$; △, $Pr = 0.5$; □, $Pr = 0.1$.

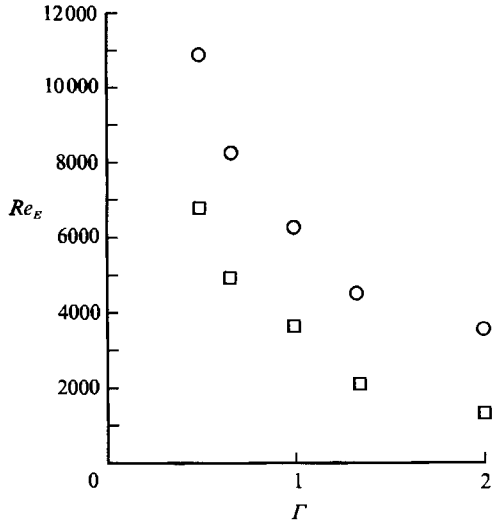

FIGURE 6. Variation of Re_E ($Gr = 0$) with Γ: ○, $Pr = 1$; □, $Pr = 0.1$.

since these results are for stability to axisymmetric disturbances, a truly definitive statement of this kind cannot be made until a subsequent analysis for non-axisymmetric disturbances is performed. It is also important to keep in mind that these sufficient conditions for stability do not imply anything about when instability will occur unless the linear and energy limits can be shown to coincide.

Another conjecture made by Xu & Davis (1984), however, appears to be borne out by the present results. As mentioned in § 1, the smaller the aspect ratio of a half-zone, the smaller the class of disturbances capable of perturbing it. Calculations for $0.5 \leqslant \Gamma \leqslant 2$ for two values of Pr and fixed Gr show a marked increase in Re_E for decreasing Γ (figure 6). A comparison of the present energy-stability results with the large-Γ, linear-theory results of Xu & Davis is desirable. However, while basic-state computations for $\Gamma = 5$ yielded velocity profiles in the middle of the half-zone which are in excellent agreement with the analytical solution of Xu & Davis (1983), sufficient resolution is unavailable to perform meaningful stability calculations for a zone this long.

It is also desirable to have results available for a wide range of all parameters present in the half-zone problem. In particular, to bridge the gap between high-Pr model experiments and low-Pr crystal melts, attempts were made to calculate energy-stability limits for Prandtl numbers higher than unity. As seen in table 3, however, this process breaks down for $Pr > 1.6$. The reason behind this appears to be the fact that $Re_E(Pr = 1.6) = 7170$, which means that $Ma_E(Pr = 1.6) = 11470$, and the calculation of the basic state is failing to converge for the apparently higher Marangoni numbers associated with even larger Prandtl numbers. The calculation of Re_E for $Pr = 1$, $\Gamma = 0.5$ also resulted in a high value for Re_E, but in this case the basic-state calculation was achieved relatively easily since increased resolution was possible in this smaller aspect-ratio zone.

Finally, figure 7 presents a comparison between the experimental results of Preisser *et al.* (1983) and the theoretical results obtained for zero Grashof number and unit Prandtl number. The experimental results of Kamotani *et al.* (1984), for $Pr = 42$ and 64, lie above the results of Preisser *et al.* The experimental results have been

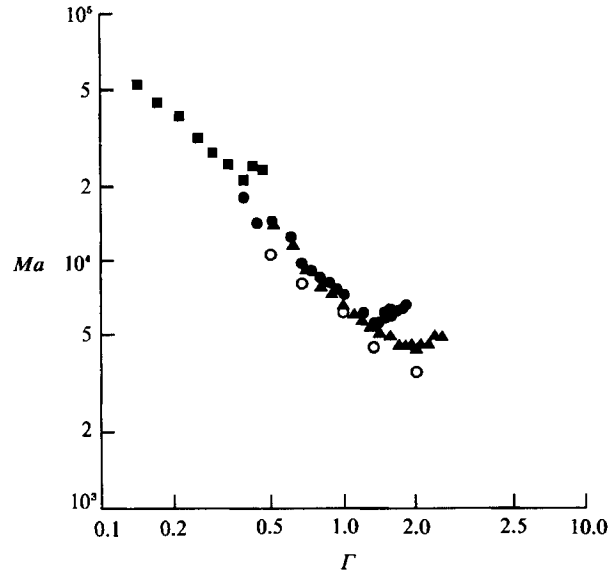

FIGURE 7. Comparison between result of present computations and model experiments. Present: ○, Me_E for axisymmetric disturbances with $Pr = 1$. Preisser *et al.* (1984): ▲, (radius = 2 mm); ●, (3 mm); ■, (10 mm).

rescaled, using the radius R of the zone as the lengthscale appearing in the expression for the Marangoni number. While at first sight the agreement appears to be excellent, it must be kept in mind that: (i) the theoretical results allow only axisymmetric perturbations; and (ii) the experiments are for a high-Pr fluid (7 for sodium nitrate (D. Schwabe, private communication)). If Ma_E continues to increase monotonically with Prandtl number as it does for the limited range of Pr computed, then results for Prandtl numbers corresponding to those of the experiments would clearly lie above the experimental data. This behaviour may imply any of the following about the theoretical and experimental results: (i) non-axisymmetric disturbances are indeed the 'most dangerous' modes; (ii) the assumption of an undeformable free surface is too restrictive; or (iii) the physical properties of the fluids used to construct the Marangoni number from the experimental data are incorrect. With regard to this last matter, the most uncertain of these properties is γ, the rate of decrease of surface tension with temperature. However, more routinely measured properties are also subject to change as evidenced by the fact that the above-quoted $Pr = 7$ for sodium nitrate differs from the value of 8.9 reported by Preisser *et al.*

What is clear from the present results is that the computed energy-stability limits are not conservative in the sense of yielding an absurdly low boundary for guaranteeing stability. Calculations of energy stability limits allowing for non-axisymmetric disturbances and a deformable free surface are clearly warranted. Ultimately, it is hoped that energy-stability calculations for a realistic model of an actual float zone allowing for melting/freezing and radiant heating will yield results which allow the crystal grower to better control the process and grow striation-free material.

The authors wish to acknowledge helpful discussions with several colleagues, in particular, Professors S. H. Davis, G. M. Homsy and D. Schwabe, and Dr P. J. Roache. This work was supported by the Microgravity Science and Applications

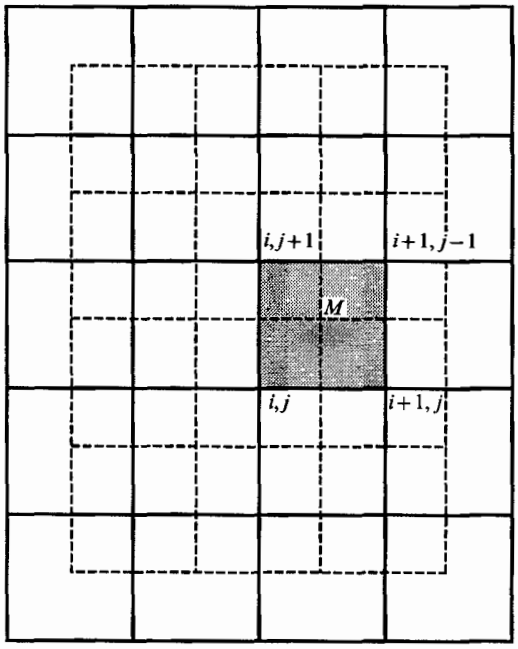

FIGURE 8. Computational grids used in the stability calculations. Solid grid is for u', w', T'; dashed grid is for π.

Division of NASA under grant NAG-3-568. G.P.N. also acknowledges support from the National Science Foundation (MSM 83-51490) and H.D.M. support from the Air Force Office of Scientific Research (AFOSR 84-0315).

Appendix. Discretization scheme

The solution region is divided into subdomains as shown in figure 8, where the mesh for the π_i terms is staggered from the mesh for the other dependent variables. The gradients in the dissipation integral are expressed at the centre of each subdomain using the average values of two central-difference approximations along relevant lines. For instance, on the subdomain shown in the figure, the dissipation terms are approximated as

$$\int_M \left(\frac{\partial u}{\partial r}\right)^2 \mathrm{d}V \approx \left[\frac{1}{2}\left(\frac{u_{i+1,j}-u_{i,j}}{\Delta r}+\frac{u_{i+1,j+1}-u_{i,j+1}}{\Delta r}\right)\right]^2 r_{\mathrm{m}}\,\Delta r\,\Delta z,$$

where the subscript m means the quantity is evaluated at the midpoint of subdomain M. Similar approximations were used for z-derivative terms.

To approximate the production terms, we use the average of each quantity on subdomain M and multiply by the basic-state velocity/temperature gradient at the centre of M, e.g.

$$\int_M u^2 \frac{\partial U}{\partial r}\,\mathrm{d}V \approx [\tfrac{1}{4}(u_{i,j}+u_{i,j+1}+u_{i+1,j}+u_{i+1,j+1})]^2 \left.\frac{\partial U}{\partial r}\right|_{\mathrm{m}} r_{\mathrm{m}}\,\Delta r\,\Delta z.$$

The integral imposing the continuity constraint is approximated as

$$\int_M \pi \nabla \cdot \boldsymbol{u}' \, \mathrm{d}V \approx \pi_{\mathrm{m}} \left[\left(\frac{u_{i+1,j} r_{i+1} - u_{i,j} r_i}{2\Delta r} + \frac{u_{i+1,j+1} r_{i+1} - u_{i,j+1} r_i}{2\Delta r} \right) + \left(r_{\mathrm{m}} \frac{w_{i,j+1} - w_{i,j}}{2\Delta z} + r_{\mathrm{m}} \frac{w_{i+1,j+1} - w_{i+1,j}}{2\Delta z} \right) \right] \Delta r \, \Delta z.$$

The surface integrals are treated in a similar way, i.e.

$$\int_{M_{\mathrm{s}}} w \frac{\partial \phi}{\partial z} \mathrm{d}z \approx \tfrac{1}{2}(w_{I,j} + w_{I,j+1}) \left(\frac{\phi_{I,j+1} - \phi_{I,j}}{\Delta z} \right) \Delta z$$

$$\int_{M_{\mathrm{s}}} Bi \, \phi^2 \, \mathrm{d}z \approx \tfrac{1}{4} Bi \, (\phi_{I,j} + \phi_{I,j+1})^2 \, \Delta z.$$

where the subscript M_{s} identifies the free-surface portion of subdomain M.

REFERENCES

AITKEN, A. C. 1926 On Bernoulli's numerical solution of algebraic equations. *Proc. R. Soc. Edinb.* **46**, 289.

BANK, R. & MITTELMANN, H. D. 1986 Continuation and multigrid for nonlinear elliptic systems. In *Multigrid Methods II* (ed. W. Hackbusch & U. Trottenberg). Lecture Notes in Mathematics, vol. 1228. Springer.

CHANG, C. E. & WILCOX, W. R. 1976 Analysis of surface tension driven flow in floating zone melting. *Intl J. Heat Mass Transfer* **19**, 335.

CHARLSON, G. S. & SANI, R. L. 1970 Thermoconvective instability in a bounded cylindrical fluid layer. *Intl J. Heat Mass Transfer* **13**, 1479.

CHUN, C.-H. 1980 Experiments on steady and oscillatory temperature distribution in a floating zone due to the Marangoni convection. *Acta Astronautica* **7**, 479.

CLARK, P. A. & WILCOX, W. R. 1976 Influence of gravity on thermocapillary convection in floating zone melting of silicon. *J. Cryst. Growth* **50**, 461.

DAVIS, S. H. 1969 Buoyancy-surface tension instability by the method of energy. *J. Fluid Mech.* **39**, 347.

DAVIS, S. H. & HOMSY, G. M. 1980 Energy stability theory for free-surface problems: buoyancy-thermocapillary layers. *J. Fluid Mech.* **98**, 527.

DAVIS, S. H. & KERCZEK, C. VON 1973 A reformulation of energy stability theory. *Arch. Rat. Mech. Anal.* **52**, 112.

FU, B. & OSTRACH, S. 1985 Numerical solution of thermocapillary flows in floating zones. In *Transport Phenomena in Materials Processing, Power Engng Div.* vol. 10, *Heat Transfer Div.* vol. 29, p. 1. ASME.

JOSEPH, D. D. 1976 *Stability of Fluid Motions I, II.* Springer.

KAMOTANI, Y., OSTRACH, S. & VARGAS, M. 1984 Oscillatory thermocapillary convection in a simulated float-zone configuration. *J. Cryst. Growth* **66**, 83.

KUHLMANN, H. 1989 Small amplitude thermocapillary flow and surface deformations in a liquid bridge. *Phys. Fluids* A **1**, 672.

MUNSON, B. R. & JOSEPH, D. D. 1971 Viscous incompressible flow between concentric rotating spheres. Part 2. Hydrodynamic stability. *J. Fluid Mech.* **49**, 305.

NEITZEL, G. P. 1984 Numerical computation of time-dependent Taylor-vortex flows in finite-length geometries. *J. Fluid Mech.* **141**, 51.

NEITZEL, G. P. & DAVIS, S. H. 1981 Centrifugal instabilities during spin-down to rest in finite cylinders. Numerical experiments. *J. Fluid Mech.* **126**, 545.

PREISSER, F., SCHWABE, D. & SHARMANN, A. 1983 Steady and oscillatory thermocapillary convection in liquid columns with free cylindrical surface. *J. Fluid Mech.* **126**, 545.

SCHWABE, D., PREISSER, F. & SCHARMANN, A. 1982 Verification of the oscillatory state of thermocapillary convection in a floating zone under low gravity. *Acta Astronautica* **9**, 265.

SEN, A. K. & DAVIS, S. H. 1982 Steady thermocapillary flow in two-dimensional slots. *J. Fluid Mech.* **121**, 163.

SMITH, M. K. 1986*a* Thermocapillary and centrifugal-buoyancy-driven motion in a rapidly rotating liquid cylinder. *J. Fluid Mech.* **166**, 245.

SMITH, M. K. 1986*b* Instability mechanisms in dynamic thermocapillary liquid layers. *Phys. Fluids* **29**, 3182.

SMITH, M. K. & DAVIS, S. H. 1983*a* Instabilities of dynamic thermocapillary liquid layers Part 1. Convective instabilities. *J. Fluid Mech.* **132**, 119.

SMITH, M. K. & DAVIS, S. H. 1983*b* Instabilities of dynamic thermocapillary liquid layers Part 2. Surface wave instabilities. *J. Fluid Mech.* **132**, 132.

XU, J.-J. & DAVIS, S. H. 1983 Liquid bridges with thermocapillarity. *Phys. Fluids* **26**, 2880.

XU, J.-J. & DAVIS, S. H. 1984 Convective thermocapillary instabilities in liquid bridges. *Phys. Fluids* **27**, 1102.

XU, J.-J. & DAVIS, S. H. 1985 Instability of capillary jets with thermocapillarity. *J. Fluid Mech.* **161**, 1.

YAMAGUCHI, Y., CHANG, C. J. & BROWN, R. 1984 Multiple buoyancy-driven flows in a vertical cylinder heated from below. *Phil. Trans. R. Soc. Lond.* A **312**, 519.

ZEBIB, A., HOMSY, G. M. & MEIBURG, E. 1985 High Marangoni number convection in a square cavity. *Phys. Fluids* **28**, 3467.